

Dynamics of water imbibition in multilayered paper channels

Sooyoung Chang, Hyunwoong Kang, Simon Song and Wonjung Kim^{3,4}

Corresponding author: Wonjung Kim, wjk@yonsei.ac.kr

(Received 15 May 2025; revised 18 August 2025; accepted 22 September 2025)

Microfluidic paper-based analytical devices ($\mu PADs$) have gained considerable attention due to their ability to transport fluids without external pumps. Fluid motion in $\mu PADs$ is driven by capillary forces through the network of pores within paper substrates. However, the inherently low flow speeds resulting from the small pore sizes in paper often limit the performance of $\mu PADs$. Recent studies have introduced multilayered $\mu PADs$ composed of stacked paper sheets, which enable significantly faster fluid transport through inter-layer channels. In this study, we present a combined theoretical and experimental investigation of water imbibition dynamics through channels formed by multiple paper layers. Upon contact with water, the paper layers absorb water and undergo swelling, altering channel geometry and consequently affecting flow dynamics. We develop a mathematical model that extends the classical Washburn equation to incorporate the effects of water absorption and swelling. The model predictions show excellent agreement with experimental observations of water flow through multilayered paper channels. The results elucidate how water absorption and swelling influence capillary imbibition, and suggest potential strategies for regulating flow rates in multilayered $\mu PADs$.

Key words: microfluidics, capillary flows, wetting and wicking

1. Introduction

Since paper was introduced as a platform for bioassays Martinez *et al.* (2007), microfluidic paper-based analytical devices (μ PADs) have attracted considerable attention due to

© The Author(s), 2025. Published by Cambridge University Press. This is an Open Access article, distributed under the terms of the Creative Commons Attribution licence (https://creativecommons.org/licenses/by/4.0/), which permits unrestricted re-use, distribution and reproduction, provided the original article is properly cited.

¹Department of Mechanical Engineering, Sogang University, Seoul 04107, Republic of Korea

²Department of Mechanical Convergence Engineering, Hanyang University, Seoul 04763, Republic of Korea

³School of Mechanical Engineering, Yonsei University, Seoul 03722, Republic of Korea

⁴Department of Battery Engineering, Yonsei University, Seoul 03722, Republic of Korea

their potential for low-cost, point-of-care diagnostics. Unlike conventional microfluidic devices that rely on micromachined structures, μ PADs utilise paper substrates capable of spontaneously imbibing water through capillary action. This passive fluid transport mechanism enables μ PADs to function without external pumps, making them particularly suitable for portable applications such as medical diagnostics, food safety monitoring, and environmental assessments (Martinez *et al.* 2010; Yetisen, Akram & Lowe 2013; Cate *et al.* 2015; Ozer, McMahon & Henry 2020).

Despite these advantages, µPADs are often limited by low flow rates, which constrain their wider applicability. Fluid transport in µPADs occurs through capillary action within the interconnected pores of the cellulose fibre network. Paper typically contains pores ranging from several to tens of micrometres in size, leading to capillary flow rates that are considerably lower than those achievable in conventional microfluidic channels (Jahanshahi-Anbuhi *et al.* 2012; Schilling *et al.* 2012; Renault *et al.* 2013; Elizalde, Urteaga & Berli 2015; Castro, Rosillo & Tsutsui 2017; Chang *et al.* 2018; Chang & Kim 2020). Consequently, µPADs frequently require prolonged operation times and are prone to issues such as sample evaporation losses (Schilling *et al.* 2012; Castro *et al.* 2017).

To address these limitations, researchers have developed multilayered μPADs designed to enhance fluid transport rates (Camplisson *et al.* 2015; Adkins, Noviana & Henry 2016; Channon *et al.* 2018, 2019; Shangguan *et al.* 2018; Pradela-Filho *et al.* 2020; Soum *et al.* 2020; Seo *et al.* 2023). Unlike single-layer devices that rely on inter-fibre pores for fluid transport, multilayered systems consist of channels formed between stacked paper layers. The effective channel height is determined by the gap between the stacked paper layers, typically of the order of hundreds of micrometres, which is substantially larger than the characteristic pore size in paper. Consequently, flow speeds through these inter-layer channels can be an order of magnitude higher than those in single-layer paper devices (Jahanshahi-Anbuhi *et al.* 2012; Channon *et al.* 2018; He *et al.* 2024). Enhanced flow rates in multilayered paper devices have enabled diverse applications, including portable viscometry (Jang *et al.* 2020*a*), microfluidic mixing (Jang *et al.* 2020*b*), and sensing of enzymes, ions and biomolecules (Adkins *et al.* 2016; Shangguan *et al.* 2018; Pradela-Filho *et al.* 2020; Seo *et al.* 2023).

Washburn (1921) formulated an equation to describe capillary-driven flow through a cylindrical tube: $l = (\sigma R \cos \theta t/(2 \mu))^{1/2}$, where l is the imbibition length, σ is the surface tension, R is the tube radius, θ is the contact angle, t is time, and μ is the liquid viscosity. Assuming that the complex porous structure of paper can be approximated as a bundle of parallel cylindrical capillary tubes, the imbibition length is expressed as $l = k_w \sqrt{t}$, where k_w is a constant that scales as $(\sigma R \cos \theta/\mu)^{1/2}$. The Washburn equation has been widely applied to predict imbibition speed through paper substrates by experimentally determining k_w (Hong & Kim 2015; Lee *et al.* 2016; Jafry *et al.* 2016; Liu *et al.* 2018).

The Washburn equation has also been applied to predict the imbibition speed through channels of multilayered paper devices (Camplisson *et al.* 2015; Channon *et al.* 2018; Shangguan *et al.* 2018). This approach is justified because multilayered paper channels can be considered as capillaries where liquid transport is primarily governed by a balance between capillary forces and viscous resistance. However, several studies have reported that the Washburn equation is often inadequate for describing water imbibition within multilayered paper channels, particularly when accurate prediction of flow rates is essential for practical applications (Channon *et al.* 2019; Schaumburg & Berli 2019).

Paper absorbs water with associated volume expansion (Alava & Niskanen 2006; Lee *et al.* 2016; Kvick *et al.* 2017; Chang & Kim 2020). When water flows through a multilayered paper channel, the paper boundaries absorb water and swell, resulting in

deformation of the channel geometry. However, the Washburn equation does not account for absorption-induced swelling of paper boundaries (Chang, Jensen & Kim 2022). Consequently, discrepancies may arise when applying the Washburn equation to describe fluid transport in multilayered paper channels.

Only a few studies have addressed the dynamics of water imbibition through multilayered paper channels. Channon et al. (2019) developed a mathematical model for predicting imbibition length, with particular emphasis on viscous dissipation within the pores of paper layers. Their model demonstrated improved accuracy over the Washburn equation in describing the experimentally measured imbibition speed. Schaumburg & Berli (2019) extended the analysis by incorporating the effects of a preceding wetting front emerging within paper boundaries. Their mathematical model successfully explained the experimental results reported by Channon et al. (2018). Additionally, Soum et al. (2020) introduced a multilayered paper channel composed of a photo-paper base and a hydrophobic cover. Their study revealed that the flow speed significantly increased within the multilayered channel and, remarkably, remained constant throughout the entire imbibition process. They attributed this abnormal flow behaviour to the presence of an absorbable, hydrophilic bottom layer and a hydrophobic top cover. However, previous studies have not explicitly accounted for the effects of water absorption and swelling of paper on the flow dynamics, leaving the mechanism of water imbibition in multilayered paper channels insufficiently understood.

In the present study, we investigate capillary-driven water flow through multilayered paper channels, explicitly considering water absorption and swelling of the paper layers. We conducted experiments to measure both the volume of water absorbed by the paper and the resultant swelling-induced changes in channel geometry. Based on these observations, we developed a mathematical model for water imbibition that incorporates the effects of water absorption and swelling. The model predictions show excellent agreement with experimental measurements, elucidating the influence of absorption and volume expansion of the paper on capillary flow dynamics. This work provides new insights into the design of multilayered µPADs and other deformable microfluidic channels.

2. Experiments

Two types of commercial filter paper (Whatman grades 5 and 6) were used in the experiments. To quantify the volume of water absorbed by the papers, paper strips measuring 5 mm in width and 5 mm in length were prepared. Each strip was vertically mounted on a support and then brought into contact with a water reservoir, allowing the strip to imbibe water via capillary action. The volume of water absorbed by a paper strip was determined by measuring the change in mass of the strip before and after saturation with water. To eliminate the influence of paper expansion on the measured volume of absorbed liquid, a similar experiment was conducted using silicone oil, which can be absorbed by paper without inducing volume expansion (Chang *et al.* 2018). The masses and volumes of water and silicone oil absorbed by the paper strips, denoted as m_w and m_o , respectively, are listed in table 1. For all paper strips tested, the volume of absorbed water exceeded that of silicone oil. The densities of silicone oil and water were 0.91 and 1.0 g cm⁻³, respectively.

We fabricated multilayered paper channels using two types of commercial filter paper (Whatman grades 5 and 6), as illustrated in figure 1(a). To pattern the paper, we applied wax using a commercial wax printer (ColorQube 8870, Xerox), leaving a 3 mm wide line uncoated. The wax-patterned paper was then baked on a hot plate at 150 °C for 2 minutes to allow the wax to penetrate the paper structure. Two layers of paper were laminated using

Paper	m_w (mg)	m_o (mg)	t_c (s)	t_s (s)
Grade 5	2.9 ± 0.1	2.3 ± 0.1	0.18 ± 0.01	0.09 ± 0.01
Grade 6	3.1 ± 0.2	2.2 ± 0.1	0.17 ± 0.01	0.10 ± 0.01

Table 1. Measured parameters for multilayered channels composed of grade 5 and grade 6 paper.

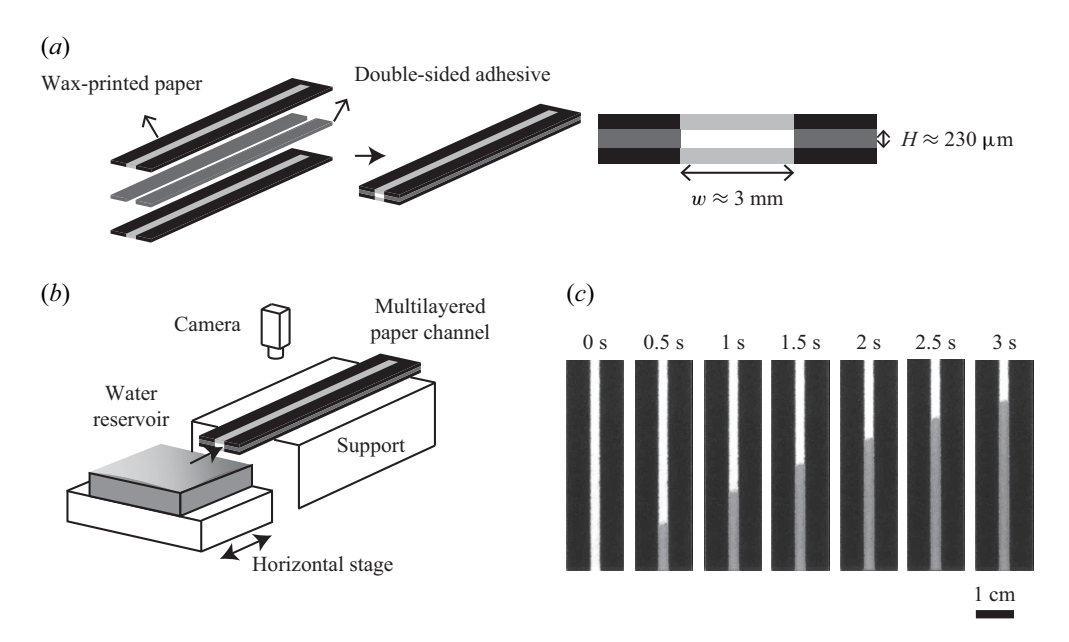


Figure 1. Schematic illustrations of (a) the fabrication process of a multilayered paper channel, and (b) the experimental set-up for measuring imbibition length through multilayered paper channels. (c) Sequential images showing water imbibition through a multilayered paper channel composed of grade 6 paper. The wet region appears darker between the black boundaries, indicating the advancing wetting front.

double-sided adhesive tape (ST-930H, Daehyun ST) with height $H \approx 230$ μ m, which served as a spacer (Channon *et al.* 2019). The thickness of the paper was 200 μ m for grade 5, and 180 μ m for grade 6.

We constructed an experimental set-up to visualise water flow through the multilayered paper channels, as depicted in figure 1(b). The multilayered paper channel was placed on a horizontal support to eliminate gravitational effects on water imbibition. Water imbibition was initiated by bringing the water reservoir into contact with the channel. The progression of the wetting front was recorded using a high-speed camera (Mini AX200, Photron). Figure 1(c) presents sequential images of the advancing wetting front during water infiltration through a grade 6 paper channel.

3. Experimental observation

We investigated water infiltration through multilayered paper channels by cutting the channels along their centreline in the longitudinal direction, and observing the flow using a high-speed camera (Mini AX200, Photron), as shown in figure 2(a). As water progressed through the channel, it rapidly infiltrated the pores of the paper layers above and below the channel. For both types of paper used, local infiltration occurred within 0.01 s. The

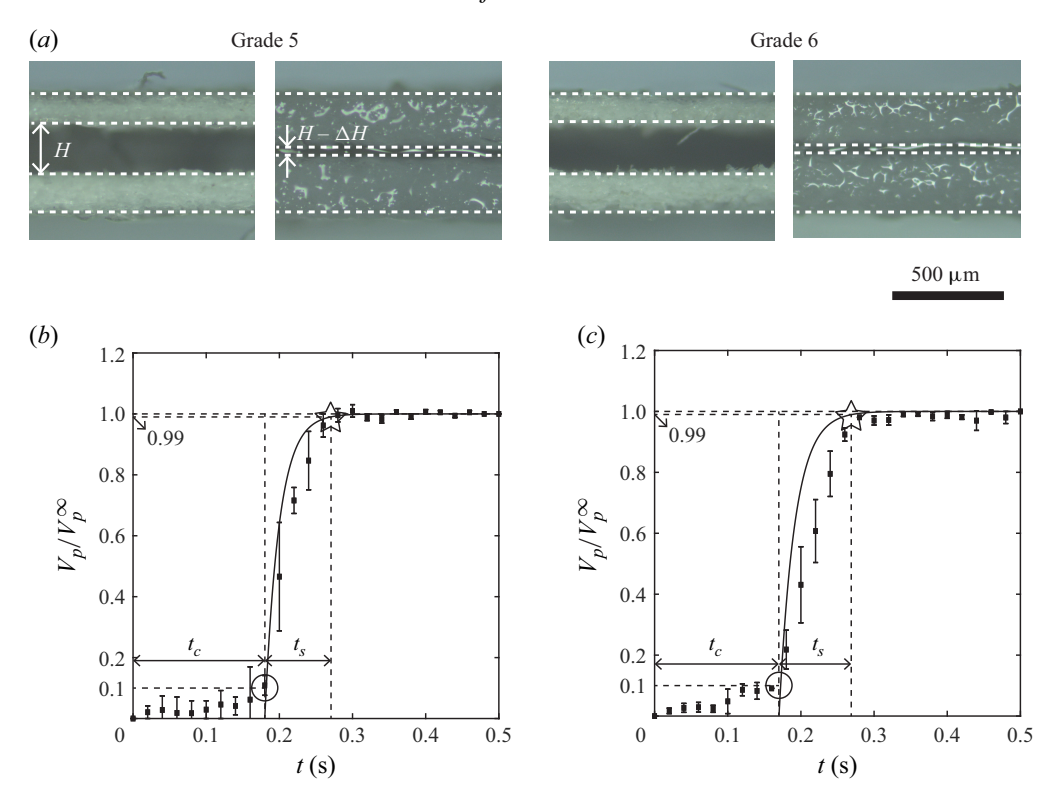


Figure 2. (a) Longitudinal section images of multilayered paper channels before and after water infiltration. Temporal variations in the volume of a single paper layer composed of (b) grade 5 paper and (c) grade 6 paper. In (b) and (c), V_p and V_p^{∞} denote the increased volume of a single paper layer and its final increased volume after complete expansion, respectively. The circle and star symbols indicate the times when the paper layer reaches 10% and 99% of its final increased volume, respectively, and t_c and t_s are the times required to reach these values, respectively. The solid lines represent (3.1).

absorption of water into the compressed cellulose fibre network induced expansion of the paper layers. The expansion followed shortly after the initial water absorption, proceeding rapidly thereafter. The swelling of the paper layers was predominantly inwards, with the final channel height reduced to approximately 10% of its initial height for both types of paper.

Figure 2(b,c) show the temporal evolution of the volume of the paper channels. We define V_p as the increased volume of a single paper layer, with V_p^{∞} representing the final increased volume after complete expansion. The volume ratio V_p/V_p^{∞} thus ranges from 0 to 1 over time. Initially, the volume ratio increased gradually, taking approximately 0.2 s to reach 0.1 for both cases. Following this initial phase, the rate of volume increase accelerated rapidly, approaching 1 within a short period.

Based on phenomenological observations of water absorption and paper swelling, we propose simple empirical equations to describe the time-dependent evolution of channel volume changes resulting from deformation of the cellulose fibre network. We define t_c as the time required for the paper layer to reach 10% of its final increased volume, indicated by circles in figure 2(b,c). For simplicity, we assume that water uptake and swelling proceed concurrently after the initial local infiltration, which occurs within approximately 0.01 s. Neglecting the initial 10% swelling during the period $0 < t < t_c$, the rapid volume

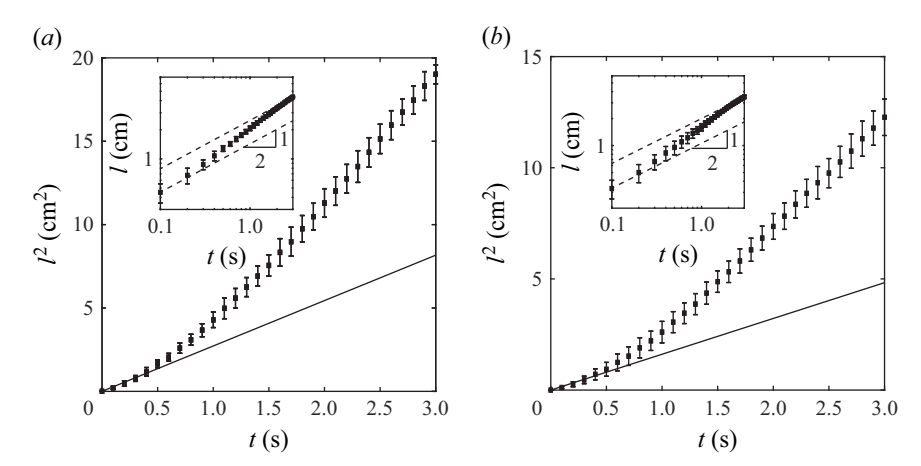


Figure 3. Dependence of l^2 on t for multilayered paper channels composed of (a) grade 5 and (b) grade 6 paper. The solid straight lines are fits to the data in the early stage (t < 0.4 s). Insets show the experimental data on a logarithmic scale. At early times, the data follow the lower asymptotic line (dotted, slope 1/2), while at later times, the imbibition length approaches the upper asymptotic line with the same slope.

increase for $t > t_c$ can be described by the exponential function (Lee et al. 2016)

$$\frac{V_p}{V_p^{\infty}} = 1 - e^{-(t - t_c)/\lambda} \quad (t > t_c),$$
 (3.1)

where λ is the time constant associated with paper swelling. Similarly, the volume of water absorbed by the expanded paper layer, V_w , can be expressed as

$$\frac{V_w}{V_w^{\infty}} = 1 - e^{-(t - t_c)/\lambda} \quad (t > t_c),$$
 (3.2)

where V_w^{∞} represents the total volume of water absorbed when the paper reaches full expansion. We further define t_s as the time required for the volume of the paper layer to reach 99 % of its final value, marked by stars in figure 2(b,c), measured from the moment $t=t_c$. For all paper grades, t_s was approximately 0.1 s. The values of t_c and t_s for each paper type are listed in table 1. In figure 2(b,c), (3.1) is represented by solid lines, which reasonably capture the characteristic rapid increase in the volume of the paper layers (see § 6 for the determination of λ).

Figure 3 presents our experimental measurements of water imbibition length through the multilayered paper channels over a period of 3 s. During the early stage (t < 0.4 s), the experimental data exhibit an approximately linear increase with respect to time, aligning well with the straight data-fitting lines. However, for t > 0.4 s, the experimental data deviate from the straight lines and curve upwards for all paper channels.

4. Theoretical analysis

We begin the theoretical analysis by constructing a geometric model that incorporates both absorption and swelling of the paper layers, as illustrated in figure 4. The side surfaces of the multilayered paper channel are neglected, as the channel width (≈ 3 mm) is much greater than its height ($\approx 230 \, \mu m$). As shown in figure 4(a), capillary-driven flow between two horizontal, impermeable plates can be analysed analogously to capillary flow in a cylindrical tube, the basis of the classical Washburn equation, since both

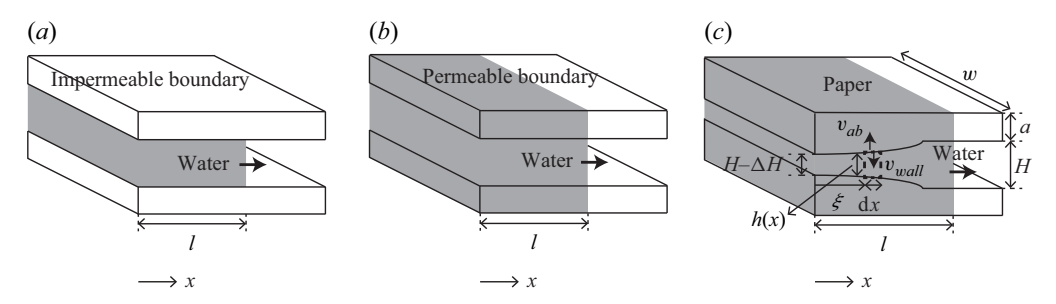


Figure 4. Model geometries for a channel with (a) an impermeable boundary, (b) a boundary that absorbs water without swelling, and (c) the present model geometry accounting for both absorption and swelling of the paper layers.

are governed by the balance between capillary forces and viscous resistance. Balancing the capillary force per unit depth, $2\sigma\cos\theta$, with the viscous resistance per unit depth, $12\ \mu ll'/H$, yields the momentum equation $l' = \sigma H\cos\theta/(6\ \mu l)$, where H is the initial channel height. Accordingly, the imbibition length can be expressed as $l = k\sqrt{t}$, where $k = (\sigma H\cos\theta/(3\ \mu))^{1/2}$.

Compared to the flow in figure 4(a), the channel boundaries in figure 4(c) can absorb water and swell, resulting in a channel height that varies along the longitudinal direction. We consider an infinitesimal segment of the channel of length dx located at a distance ξ from the channel inlet, as indicated by the dashed box in figure 4(c). Within this segment, the continuity equation for water is given by $h(du/dx) = -2(v_{ab} - v_{wall})$, where u is the local average velocity of water in the longitudinal direction, v_{ab} is the velocity of water moving into the paper boundary due to absorption, and v_{wall} is the inward velocity of the channel boundary resulting from paper swelling. Integrating the continuity equation from ξ to l yields

$$u(\xi) = l'(t) + \int_{\xi}^{l} \frac{2(v_{ab} - v_{wall})}{h} dx,$$
 (4.1)

with l' being dl/dt, and u(l) = l'(t).

The height of the channel, h, depends on the local volume expansion of the paper and is bounded below by the minimum height $H - \Delta H$. The expanded volume of the paper layer, given by $w \, \mathrm{d}x \, (H-h)$, is equal to $2V_p^\infty (1-\mathrm{e}^{-(t-\tau-t_c)/\lambda})$ from (3.1), where w is the channel width. Substituting $V_p^\infty = w \, \mathrm{d}x \, (\Delta H/2)$, the channel height h is expressed as

$$h(\xi) = H - \Delta H (1 - e^{-(t - \tau - t_c)/\lambda}),$$
 (4.2)

where τ is the time satisfying $l(\tau) = \xi$, thus implying that $t - \tau$ is the local swelling time. Since $dh/dt = -2v_{wall}$, v_{wall} is expressed as

$$v_{wall} = \begin{cases} 0 & (t - \tau < t_c), \\ \frac{\Delta H}{2\lambda} e^{-(t - \tau - t_c)/\lambda} & (t - \tau > t_c). \end{cases}$$
(4.3)

We now derive an expression for v_{ab} . To do so, we introduce the time scale t_a , which characterises the initial local infiltration of water into the pores of the paper layer. Upon contact with water, the adjacent paper layers are first saturated as water fills their pore spaces. During this initial phase $(t < t_a)$, the velocity of water entering the paper is given by $a\phi/t_a$, where a and ϕ denote the thickness and porosity of the paper, respectively. After t_a , additional water absorption occurs, accompanied by swelling of the paper layer.

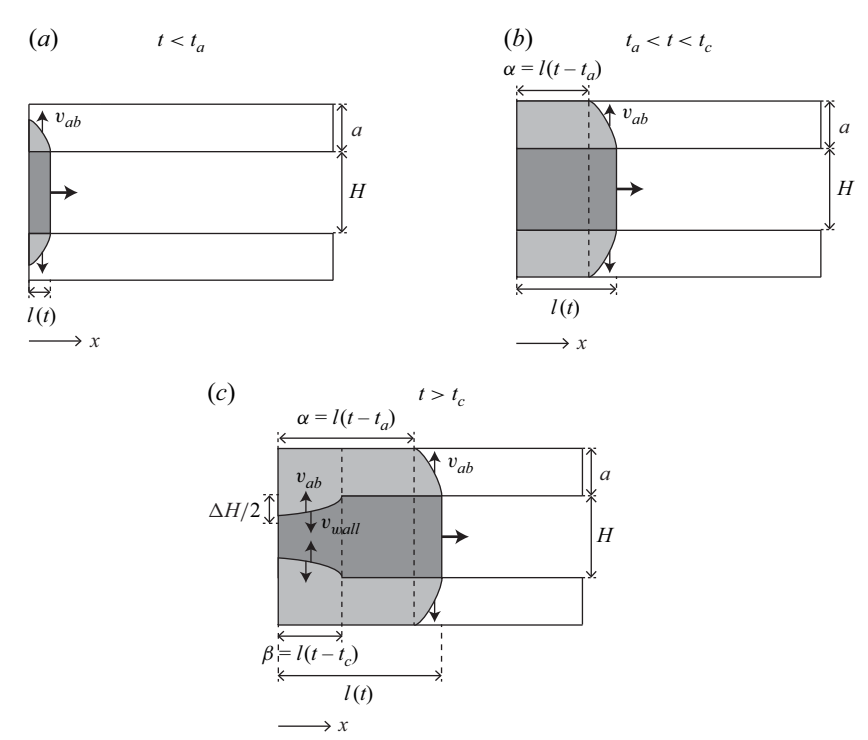


Figure 5. Schematics of the water imbibition phases for (a) $t < t_a$, (b) $t_a < t < t_c$ and (c) $t > t_c$.

The rate of water volume absorbed within the segment is given by $(w \, \mathrm{d}x)v_{ab} = \mathrm{d}V_w/\mathrm{d}t$. Combining this relation with (3.2) and $V_w^\infty = (w \, \mathrm{d}x)(\Delta H/2)$, we obtain the following expression for v_{ab} :

$$v_{ab} = \begin{cases} a\phi/t_a & (t - \tau < t_a), \\ 0 & (t_a < t - \tau < t_c), \\ \frac{\Delta H}{2\lambda} \frac{V_w^{\infty}}{V_p^{\infty}} e^{-(t - \tau - t_c)/\lambda} & (t - \tau > t_c). \end{cases}$$
(4.4)

The momentum equation for water flow in the longitudinal direction is derived from the balance between capillary force and viscous resistance. Due to water absorption and the associated volume expansion of the paper layers, the flow speed within the channel varies along the longitudinal direction. The momentum equation is given as $2\sigma\cos\theta = \int_0^l 2\Gamma \,dx$, where $\Gamma = 6\,\mu u/h$ is the local shear stress in the paper channel. One can simplify the momentum equation to

$$\int_0^l \frac{u}{h} \, \mathrm{d}x = \frac{\sigma \cos \theta}{6 \, \mu}.\tag{4.5}$$

A single governing equation for l(t) is obtained by substituting (4.1) into (4.5):

$$l'(t) \int_0^l \frac{H}{h} dx + \int_0^l \frac{H}{h} \left(\int_{\xi}^l \frac{2(v_{ab} - v_{wall})}{h} dx \right) dx = \frac{1}{2}k^2, \tag{4.6}$$

where $k = (\sigma H \cos \theta / (3 \mu))^{1/2}$. Since the water flow involves two characteristic time scales, t_a and t_c , distinct forms of the coupled equations arise in each corresponding

time regime. We first consider the case $t < t_a$ (see figure 5a). Substituting $v_{ab} = a\phi/t_a$, $v_{wall} = 0$ and h = H into (4.6) yields

$$l(t) l'(t) + \frac{a\phi}{Ht_a} \{l(t)\}^2 = \frac{1}{2}k^2, \tag{4.7}$$

where $dx = l'(\tau) d\tau$ is used.

Figure 5(b) illustrates the time regime $t_a < t < t_c$. In this period, the flow speed in the channel, $u(\xi)$, must be described by two separate expressions for the regions $0 < \xi < \alpha$ and $\xi > \alpha$, where $\alpha = l(t - t_a)$ represents the length of the paper that is fully saturated with water but has not yet undergone expansion. In the region $0 < \xi < \alpha$, we have $v_{ab} = 0$, $v_{wall} = 0$ and h = H. For $\xi > \alpha$, the conditions are $v_{ab} = a\phi/t_a$, $v_{wall} = 0$ and h = H. Substituting these expressions into (4.6) yields

$$l(t) l'(t) + \frac{a\phi}{Ht_a} \left[\{l(t)\}^2 - \{l(t - t_a)\}^2 \right] = \frac{1}{2} k^2.$$
 (4.8)

Finally, we consider the time regime $t > t_c$, as shown in figure 5(c). In this domain, the flow speed in the channel, $u(\xi)$, must be described by three different expressions over the intervals $0 < \xi < \beta$, $\beta < \xi < \alpha$ and $\xi > \alpha$, where $\beta = l(t - t_c)$ denotes the length of the region where the paper has begun to swell. In the region $0 < \xi < \beta$, the governing quantities are given by $v_{ab} = (\Delta H/(2\lambda))(V_w^\infty/V_p^\infty) e^{-(t-\tau-t_c)/\lambda}$, $v_{wall} = (\Delta H/(2\lambda)) e^{-(t-\tau-t_c)/\lambda}$ and $h = H - \Delta H (1 - e^{-(t-\tau-t_c)/\lambda})$. For $\beta < \xi < \alpha$, we use $v_{ab} = 0$, $v_{wall} = 0$ and h = H. For $\xi > \alpha$, the conditions are $v_{ab} = a\phi/t_a$, $v_{wall} = 0$ and h = H. Substituting these expressions into (4.6) yields

$$l'(t) \left\{ l(t) - l(t - t_c) + \int_0^{t - t_c} \frac{H \, l'(\tau)}{H - \Delta H \, (1 - e^{-(t - \tau - t_c)/\lambda})} \, d\tau \right\}$$

$$+ \frac{a\phi}{H t_a} \left\{ l(t) - l(t - t_a) \right\}$$

$$\times \left[l(t) + l(t - t_a) - 2l(t - t_c) + \int_0^{t - t_c} \frac{H \, l'(\tau)}{H - \Delta H \, (1 - e^{-(t - \tau - t_c)/\lambda})} \, d\tau \right]$$

$$+ \frac{\Delta H}{\lambda} \left(\frac{V_w^{\infty}}{V_p^{\infty}} - 1 \right)$$

$$\times \int_0^{t - t_c} \frac{H \, l'(\tau)}{H - \Delta H \, (1 - e^{-(t - \tau - t_c)/\lambda})} \left(\int_{\tau}^{t - t_c} \frac{l'(\tau) \, e^{-(t - \tau - t_c)/\lambda}}{H - \Delta H \, (1 - e^{-(t - \tau - t_c)/\lambda})} \, d\tau \right) d\tau$$

$$= \frac{1}{2} k^2.$$

$$(4.9)$$

In our experiments, the local infiltration time t_a , defined as the time required for the paper to become locally saturated with water prior to swelling, was measured to be less than 0.01 s. This value is approximately an order of magnitude smaller than $t_c \approx 0.2$ s for both types of paper used. Given this clear separation of time scales, we simplify the forms of (4.7), (4.8) and (4.9). In the limit $t_a \rightarrow 0$, (4.7) vanishes, while (4.8) and (4.9) reduce to

$$l(t) l'(t) \left(1 + \frac{2a\phi}{H}\right) = \frac{1}{2}k^2 \quad (t < t_c)$$
 (4.10)

Dimensionless parameter	Definition	Range	Physical meaning
ψ	$a\phi/H$	$\psi > 0$	Ratio of the void volume in the paper boundary to the volume of the main channel
ε	$\Delta H/H$	$0 < \varepsilon < 1$	Ratio of the reduced channel height to the initial channel height
ω	$V_w^{\infty}/V_p^{\infty}$	$0 < \omega < 1$	Ratio of the absorbed water volume in the expanded region of the paper layer to its total expansion volume
η	λ/t_c	$\eta > 0$	Ratio of the swelling time constant to the characteristic delay time

Table 2. Dimensionless parameters used in the model.

and

$$l'(t) \left(1 + \frac{2a\phi}{H}\right) \left\{ l(t) - l(t - t_c) + \int_0^{t - t_c} \frac{H \, l'(\tau)}{H - \Delta H \, (1 - e^{-(t - \tau - t_c)/\lambda})} \, d\tau \right\}$$

$$+ \frac{\Delta H}{\lambda} \left(\frac{V_w^{\infty}}{V_p^{\infty}} - 1 \right)$$

$$\times \int_0^{t - t_c} \frac{H \, l'(\tau)}{H - \Delta H \, (1 - e^{-(t - \tau - t_c)/\lambda})} \left(\int_{\tau}^{t - t_c} \frac{l'(\tau) \, e^{-(t - \tau - t_c)/\lambda}}{H - \Delta H \, (1 - e^{-(t - \tau - t_c)/\lambda})} \, d\tau \right) d\tau$$

$$= \frac{1}{2} k^2 \quad (t > t_c),$$

$$(4.11)$$

respectively.

We proceed by non-dimensionalising (4.10) and (4.11) using the characteristic time scale t_c and length scale $l_c = k\sqrt{t_c}$. Expressed in terms of the dimensionless variables $t^* = t/t_c$ and $l^* = l/l_c$, the governing equation becomes

$$l^*(t^*) l^{*'}(t^*) (1 + 2\psi) = \frac{1}{2} \quad (t^* < 1)$$
(4.12)

and

$$l^{*'}(t^*) (1 + 2\psi) f(t^*) + \varepsilon(\omega - 1) g(t^*) = \frac{1}{2} \quad (t^* > 1), \tag{4.13}$$

where

$$f(t^*) = l^*(t^*) - l^*(t^* - 1) + \int_0^{t^* - 1} \frac{l^{*'}(\tau^*)}{1 - \varepsilon(1 - e^{-(t^* - \tau^* - 1)/\eta})} d\tau^*$$
(4.14)

and

$$g(t^*) = \int_0^{t^*-1} \frac{l^{*'}(\tau^*)}{1 - \varepsilon(1 - e^{-(t^* - \tau^* - 1)/\eta})} \left(\int_{\tau^*}^{t^*-1} \frac{l^{*'}(\tau^*) e^{-(t^* - \tau^* - 1)/\eta}/\eta}{1 - \varepsilon(1 - e^{-(t^* - \tau^* - 1)/\eta})} d\tau^* \right) d\tau^*.$$
(4.15)

Here, $\psi = a\phi/H$ represents the ratio of the void volume in the paper boundary to the volume of the main channel, $\varepsilon = \Delta H/H$ is the ratio of the reduced channel height to the initial height, $\omega = V_w^\infty/V_p^\infty$ denotes the ratio of the absorbed water volume in the expanded region of the paper layer to its total expansion volume, and $\eta = \lambda/t_c$ is the ratio of the swelling time constant to the characteristic delay time. The dimensionless parameters are summarised in table 2.

In the time regime $t^* < 1$, (4.12) indicates that imbibition through the channel is governed solely by water loss through the channel boundaries. When $\psi = 0$, corresponding to the case where no water is absorbed into the boundaries, (4.12) reduces to the classical Washburn equation, $l^*(t^*)$ $l^{*'}(t^*) = 1/2$.

When wall swelling occurs for $t^* > 1$, the paper boundaries begin to expand locally. Because water fills the pore space within the paper boundaries as it flows, the absorbed water volume cannot exceed the expanded volume of the boundaries. This is consistent with our observation that the paper boundaries expand more than the volume of water that they retain, resulting in $0 < \omega < 1$. Comparing (4.13) with (4.12), we observe that $l^*(t^*)$ in the first term is replaced by $f(t^*)$, and an additional term, $\varepsilon(\omega - 1) g(t^*)$, is introduced. As the channel walls expand inwards, two competing effects influence the imbibition speed. First, the reduction in channel height due to swelling increases the viscous shear stress at the boundaries, thereby slowing the flow. Second, because the boundaries expand more than the volume of water they absorb, they compress the fluid within the channel and push it forwards, enhancing the imbibition speed. Therefore, the two effects represented by $f(t^*)$ and $\varepsilon(\omega - 1) g(t^*)$ respectively act in opposition to one another in determining the flow speed within the main channel.

It is worth noting several limiting cases of (4.13). When $\omega = 1$, the boundary expands by exactly the same volume as the absorbed water, causing the term $\varepsilon(\omega - 1) g(t^*)$ to vanish. In this case, only the first effect remains, represented by $f(t^*)$. The condition $\varepsilon = 0$ corresponds to a situation where the channel walls do not swell at all, as shown in figure 4(b), reducing (4.13) to the simpler form of (4.12). Likewise, as η increases, the swelling of the walls slows down. In the limit $\eta \to \infty$, (4.13) also converges to (4.12), representing a no-swelling condition (see Appendix A).

5. Numerical solution

Since the analytical solution to (4.12) is readily obtained as $l^*(t^*) = (t^*/(1+2\psi))^{1/2}$, we numerically solve the dimensionless governing equation (4.13) for given values of ψ , ε , ω and η , as detailed in the following numerical procedure.

The dimensionless time domain $(0, t_L^*)$ is discretised into n+1 nodes: $t_0^*, t_1^*, \ldots, t_n^*$ $(=t_L^*)$. We numerically solve the equation $l^{*'}(t^*)$ $(1+2\psi)$ $f(t^*)+\varepsilon(\omega-1)$ $g(t^*)=1/2$ at t_m^* , where $r+1\leqslant m\leqslant n$, and r is defined such that $t_r^*<1$ and $t_{r+1}^*>1$. Given that $l^{*'}(t^*)=\{1/2-\varepsilon(\omega-1)$ $g(t^*)\}/\{(1+2\psi)$ $f(t^*)\}$, integration of the equation from t_{m-1}^* to t_m^* yields.

$$\int_{l^*(t_{m-1}^*)}^{l^*(t_m^*)} dl^* = \int_{t_{m-1}^*}^{t_m^*} \left[\frac{\{1/2 - \varepsilon(\omega - 1) g(t^*)\}}{\{(1 + 2\psi) f(t^*)\}} \right] dt^*$$
 (5.1)

The numerical integration results in a simple recursive relation $l^*(t_m^*) \approx l^*(t_{m-1}^*) + [\{1/2 - \varepsilon(\omega - 1) \ g(t_m^*)\}/\{(1 + 2\psi) \ f(t_m^*)\}] \ \delta t^*$, where $\delta t^* = t_L^*/n$. The values of $f(t_m^*)$ and $g(t_m^*)$ are computed via numerical integration of the discretised governing equations, given by

$$f(t_m^*) = l^*(t_{m-1}^*) + l^*(t_{m-r}^*) + \left\{ \sum_{j=0}^{m-r} \frac{l^{*'}(t_j^*)}{1 - \varepsilon(1 - e^{-(t_m^* - t_j^* - t_r^*)/\eta})} \right\} \times (\delta t^*)$$
 (5.2)

Paper	$k \text{ (mm s}^{-1/2})$	ψ	ε	ω	η
Grade 5	22.62	0.44	0.86	0.18	0.10
Grade 6	17.30	0.43	0.87	0.20	0.13

Table 3. Estimations of experimental parameters of our model for each multilayered paper channel.

and

$$g(t_m^*) = \left[\sum_{j=0}^{m-r} \left\{ \frac{l^{*'}(t_j^*)}{1 - \varepsilon (1 - e^{-(t_m^* - t_j^* - t_r^*)/\eta})} \left(\sum_{i=j}^{m-r} \frac{l^{*'}(t_i^*) e^{-(t_m^* - t_i^* - t_r^*)/\eta}/\eta}{1 - \varepsilon (1 - e^{-(t_m^* - t_i^* - t_r^*)/\eta})} \right) \right\} \right] \times (\delta t^*)^2.$$
(5.3)

Sequential calculations can be initiated from t_{r+1}^* , yielding results for $l^*(t_{r+1}^*)$ to $l^*(t_L^*)$.

6. Results and discussion

The imbibition lengths for the two types of paper listed in table 1 are predicted using (4.12) and (4.13). This prediction requires experimental determination of several intrinsic material properties, expressed in terms of the four dimensionless parameters summarised in table 2.

We first describe the procedure for determining ψ . From the measured mass of silicone oil absorbed by the paper strip, m_o , we calculated the absorbed silicone oil volume. The porosity ϕ was then obtained by dividing this volume by the initial volume of the paper strip, which was calculated using the known paper thickness and the channel width. The dimensionless volume ratio ψ was evaluated as $a\phi/H$.

The swelling ratio ε was determined by directly measuring the change in channel height, as shown in figure 2(a), and normalising it by the initial channel height.

To evaluate ω , we measured the absorbed masses of silicone oil (m_o) and water (m_w) in the paper strips after full saturation. The volume of water ultimately absorbed in the expanded portion of the paper boundary, denoted as V_w^{∞} , was calculated as the difference between the final absorbed volumes of water and silicone oil. The final expansion volume of the paper, V_p^{∞} , was obtained from the measured thickness change for both grade 5 and grade 6 papers (Chang & Kim 2020). The parameter ω was then determined as the ratio $V_w^{\infty}/V_p^{\infty}$ for each paper type.

From the time-dependent volume measurements shown in figure 2, we also determined $\eta = \lambda/t_c$. By applying the condition $V_p \approx 0.99 V_p^{\infty}$ at $t = t_c + t_s$ to (3.1), the time constant for volume expansion was estimated as $\lambda \approx t_s/4.6$. Using the experimentally measured values of t_c and t_s listed in table 1, we then calculated η .

Finally, we determined k_{ab} , the proportionality constant in (4.12). Compared to the original Washburn constant k, the adjusted constant is given by $k_{ab} = k/\sqrt{1+2\psi}$. As shown in figure 3, both experimental curves approximately follow the prediction of (4.12) for t < 0.4 s, suggesting that paper swelling has a negligible effect in this early phase. Therefore, we estimated k_{ab} from the slope of the experimental data during the initial stage for both paper types, and subsequently obtained k using the measured value of k. All measured parameters are listed in table 3.

Figure 6 presents a comparison between experimental measurements and model predictions for water imbibition through multilayered paper channels. The experimental results show good agreement with the model, exhibiting a faster imbibition rate than the prediction based solely on water absorption through the pores of the paper layers, which is

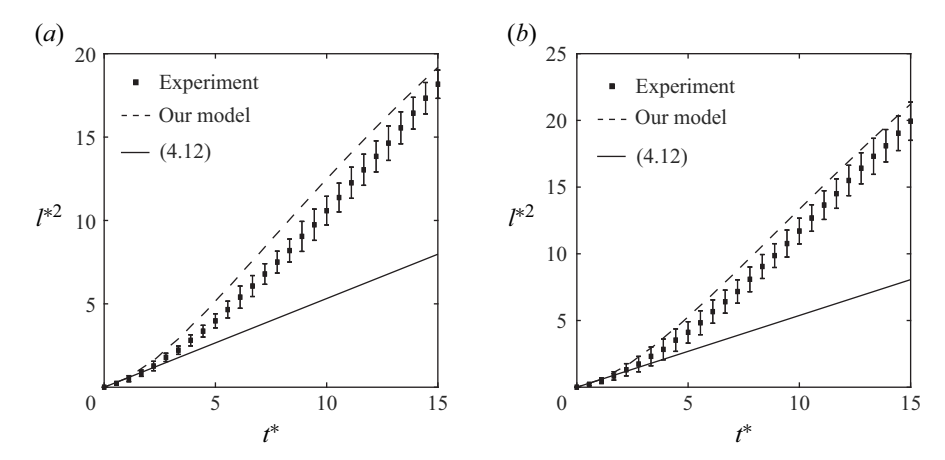


Figure 6. Comparison between model predictions and experimental results for channels made of (a) grade 5 and (b) grade 6 paper.

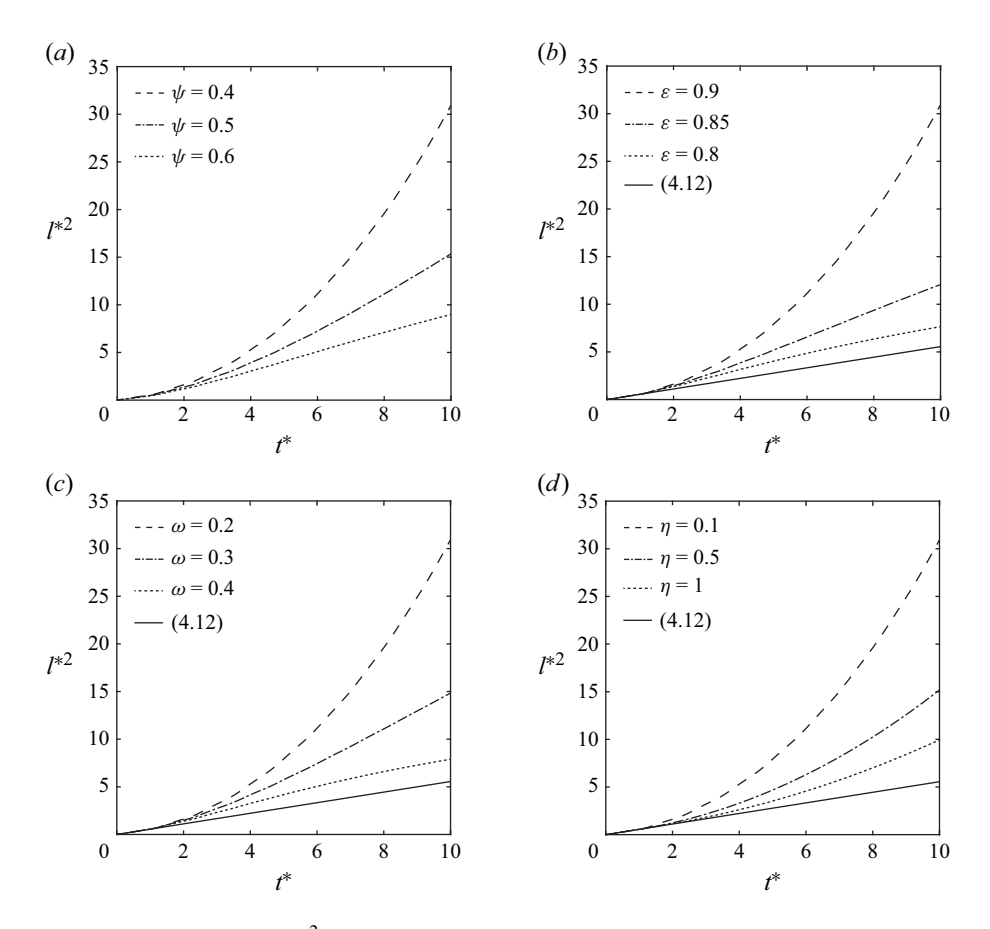


Figure 7. Model predictions of t^{*2} on t^{*} for varying values: (a) $0.4 < \psi < 0.6$, (b) $0.8 < \varepsilon < 0.9$, (c) $0.2 < \omega < 0.4$, and (d) $0.1 < \eta < 1$. In all plots, parameters are fixed at $\psi = 0.4$, $\varepsilon = 0.9$, $\omega = 0.2$ and $\eta = 0.1$, except for the one being varied in each case.

represented by the solid lines. This highlights the importance of accounting for both water absorption and the swelling of paper layers when predicting flow speed in multilayered paper channels. These effects are effectively captured by the dimensionless parameters ψ , ε , ω and η in our model.

We discuss the dependence of the model predictions on the four dimensionless parameters. Figure 7 presents numerical results of l^{*2} as a function of t^* for the ranges $0.4 < \psi < 0.6, 0.8 < \varepsilon < 0.9, 0.2 < \omega < 0.4$ and $0.1 < \eta < 1$. These ranges were selected to encompass the experimentally measured values of the corresponding dimensional parameters for both types of paper. In all plots, the parameters are fixed at $\psi = 0.4$, $\varepsilon = 0.9$, $\omega = 0.2$ and $\eta = 0.1$, except for the parameter being varied in each case. The solid lines represent the solution to (4.12), corresponding to the limiting case $\eta \to \infty$ or $\varepsilon = 0$, where no swelling occurs. In figure 7(a), the solid line corresponding to (4.12) is omitted, as it depends on the varying value of ψ in the plot. During the early phase ($t^* < 1$), all curves (dashed and dotted lines) closely follow the solid line. For $t^* > 1$, as the channel walls begin to swell, the imbibition speed becomes sensitive to the values of ψ , ε , ω and η .

Figure 7(a) shows that the imbibition speed decreases as ψ increases. This occurs because more water is diverted to the paper boundaries with increasing ψ , thereby reducing the volume of water transported through the main channel. Figure 7(b) illustrates the effect of volumetric expansion of the paper and the associated narrowing of the channel as ε increases. While a larger ε results in greater channel constriction and thus higher viscous resistance, the expanding walls may also compress the fluid and drive it forwards. This squeezing effect can dominate the increased resistance, particularly in the range considered here. Similarly, as ω decreases, the expanded volume of the channel wall becomes larger relative to the absorbed water volume, enhancing the forward flow and resulting in a higher imbibition speed, as shown in figure 7(c). Finally, figure 7(d) presents the effect of η , which characterises the swelling rate. A smaller η , corresponding to faster wall expansion, leads to a greater imbibition length at a given time. In figure 7, all curves eventually converge to straight lines at later times. This occurs because the squeezing effect of the paper boundaries becomes negligible once the layers are fully swollen in most regions behind the wetting front, leaving swelling active only near the front itself. As a result, the imbibition length recovers the $l \sim t^{1/2}$ scaling but with a modified prefactor that reflects the altered channel geometry in the swollen state. This long-time behaviour is consistent with the experimental results shown in the insets of figure 3, where the data approach two asymptotic lines with the same slope 1/2.

Figure 8 presents a contour plot of the imbibition length after 3 s, as predicted by our model, as a function of ε and ω , with fixed values k=15 mm s^{-1/2}, $\psi=0.4$ and $\eta=0.1$. The contours show that longer imbibition lengths occur in regions with low ω and high ε . Interestingly, the effect of increasing wall expansion on imbibition length varies significantly depending on the value of ω . For example, at $\omega=0.1$, increasing ε from 0.6 to 0.9 more than doubles the imbibition length, from 1.8 to 4 cm. In contrast, for larger values of ω , imbibition length decreases with increasing ε . At $\omega=0.8$, increasing ε from 0.2 to 0.9 results in a decrease in imbibition length from 1.8 to 1 cm.

This behaviour arises from the interplay between wall expansion and water absorption. When ω is small, the volume of water absorbed by the paper boundary is relatively small compared to the expanded volume of the wall. In this case, the squeezing effect of wall expansion dominates, accelerating the flow despite the associated increase in viscous resistance. However, when ω is large, the squeezing effect becomes negligible, and the increase in viscous resistance due to wall expansion becomes dominant, leading to slower imbibition. As a result, at high values of ω , the imbibition speed decreases with increasing ε .

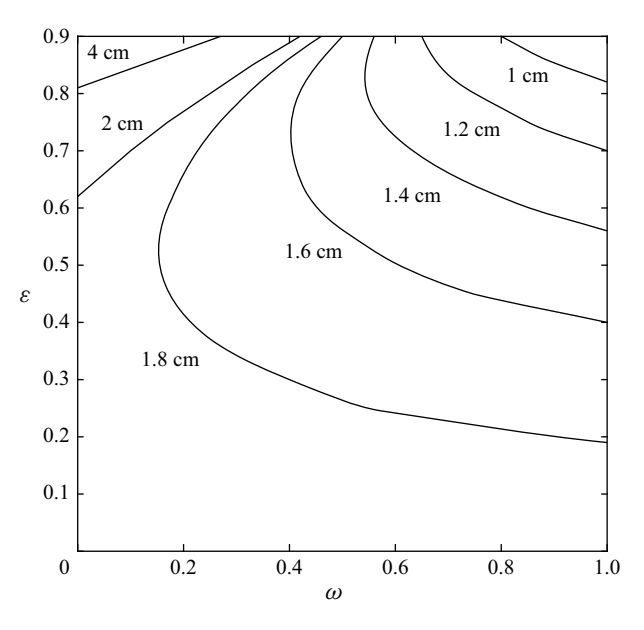


Figure 8. Contour plot showing the imbibition length after 3 s, predicted by the model as a function of ε and ω , with fixed parameters k = 15 mm s^{-1/2}, $\psi = 0.4$ and $\eta = 0.1$.

The present model uncovers a novel mechanism for regulating capillary-driven flow in microfluidic systems, based on the absorption and swelling behaviour of the channel boundaries. In contrast to conventional strategies that rely on modifying channel geometry or surface wettability (Fu & Downs 2017; Olanrewaju *et al.* 2018), our results suggest that flow control can be achieved solely by tuning the material properties of the channel walls. This introduces an alternative approach to flow regulation, particularly suited for pump-free microfluidic platforms that require rapid and consistent fluid transport.

The model reveals that under certain parameter combinations, the imbibition speed does not necessarily decrease over time as predicted by classical theory. Instead, the flow rate can remain constant or even accelerate. For example, in channels with large ε and small ω , the expansive motion of the boundaries can outweigh the increase in viscous resistance, resulting in a net enhancement of flow. This behaviour challenges the conventional expectation that capillary-driven flow inevitably slows with time. Furthermore, swelling-enhanced transport may help to explain previously reported deviations in imbibition dynamics (Songok & Toivakka 2016; Soum *et al.* 2020; Li *et al.* 2021), where measured flow rates exceeded those predicted by models assuming rigid or purely absorptive boundaries.

7. Conclusion

We have investigated the dynamics of capillary imbibition in multilayered paper channels, focusing on the roles of water absorption and swelling of the paper substrate. Experimental observations revealed that upon contact with water, the paper layers composing the channel boundaries undergo both liquid uptake and volumetric expansion, which significantly influence the flow dynamics. Building on these observations, we developed a mathematical model that incorporates the coupled effects of water absorption and swelling-induced deformation. The model predictions are in good agreement with experimental measurements, capturing the key features of imbibition behaviour across a range of material parameters. This work clarifies the physical mechanisms by which boundary

deformability alters capillary flow in paper-based microfluidic systems. In addition to providing a theoretical framework for understanding fluid transport in multilayered paper channels, our results suggest new strategies for designing $\mu PADs$ with enhanced and tunable flow characteristics. The model may also be extended to a broader class of soft microfluidic systems, where robust and precise control of flow speed is required.

Funding. This research was supported by grants from the National Research Foundation of Korea (NRF) funded by the Korean government (MSIT) (RS-2024-00334475).

Declaration of interests. The authors report no conflict of interest.

Appendix A. Derivation of (4.13) in the limit $\eta \to \infty$

In (4.13), we first derive $\lim_{\eta\to\infty} f(t^*)$. Since $\lim_{\eta\to\infty} e^{-(t^*-\tau^*-1)/\eta} = 1$, we have

$$\lim_{\eta \to \infty} f(t^*) = \lim_{\eta \to \infty} \left\{ l^*(t^*) - l(t^* - 1) + \int_0^{t^* - 1} \frac{l^{*'}(\tau^*)}{1 - \varepsilon(1 - e^{-(t^* - \tau^* - 1)/\eta})} d\tau^* \right\}$$
(A1)
$$= l^*(t^*) - l(t^* - 1) + l(t^* - 1)$$

$$= l^*(t^*).$$

We now derive $\lim_{\eta\to\infty} g(t^*)$. Since $\lim_{\eta\to\infty} e^{-(t^*-\tau^*-1)/\eta}/\eta = 0$, we have

$$\lim_{\eta \to \infty} g(t^*) = \lim_{\eta \to \infty} \left\{ \int_0^{t^* - 1} \frac{l^{*'}(\tau^*)}{1 - \varepsilon (1 - e^{-(t^* - \tau^* - 1)/\eta})} \times \left(\int_{\tau^*}^{t^* - 1} \frac{l^{*'}(\tau^*) e^{-(t^* - \tau^* - 1)/\eta}/\eta}{1 - \varepsilon (1 - e^{-(t^* - \tau^* - 1)/\eta})} d\tau^* \right) d\tau^* \right\}$$

$$= 0$$
(A2)

Plugging (A1) and (A2) into (4.13), we deduce that (4.13) converges to (4.12) as $\eta \to \infty$.

REFERENCES

ADKINS, J.A., NOVIANA, E. & HENRY, C.S. 2016 Development of a quasi-steady flow electrochemical paper-based analytical device. *Anal. Chem.* 88, 10639–10647.

ALAVA, M. & NISKANEN, K. 2006 The physics of paper. Rep. Prog. Phys. 69, 669-723.

CAMPLISSON, C.K., SCHILLING, K.M., PEDROTTI, W.L., STONE, H.A. & MARTINEZ, A.W. 2015 Two-ply channels for faster wicking in paper-based microfluidic devices. *Lab on a Chip* 15, 4461–4466.

CASTRO, C., ROSILLO, C. & TSUTSUI, H. 2017 Characterizing effects of humidity and channel size on imbibition in paper-based microfluidic channels. *Microfluid. Nanofluid.* 21, 21.

CATE, D.M., ADKINS, J.A., METTAKOONPITAK, J. & HENRY, C.S. 2015 Recent developments in paper-based microfluidic devices. *Anal. Chem.* 87, 19–41.

CHANG, S., JENSEN, K.H. & KIM, W. 2022 Dynamics of water imbibition through hydrogel-coated capillary tubes. Phys. Rev. Fluids 7, 064301.

CHANG, S. & KIM, W. 2020 Dynamics of water imbibition through paper with swelling. J. Fluid Mech. 892, A39.

CHANG, S., SEO, J., HONG, S., LEE, D.-G. & KIM, W. 2018 Dynamics of liquid imbibition through paper with intra-fibre pores. *J. Fluid Mech.* **845**, 36–50.

CHANNON, R.B., NGUYEN, M.P., HENRY, C.S. & DANDY, D.S. 2019 Multilayered microfluidic paper-based devices: characterization, modeling, and perspectives. *Anal. Chem.* 91, 8966–8972.

CHANNON, R.B., NGUYEN, M.P., SCORZELLI, A.G., HENRY, E.M., VOLCKENS, J., DANDY, D.S. & HENRY, C.S. 2018 Rapid flow in multilayer microfluidic paper-based analytical devices. *Lab on a Chip* 18, 793–802.

ELIZALDE, E., URTEAGA, R. & BERLI, C.L.A. 2015 Rational design of capillary-driven flows for paper-based microfluidics. *Lab on a Chip* 15, 2173–2180.

- FU, E. & DOWNS, C. 2017 Progress in the development and integration of fluid flow control tools in paper microfluidics. Lab on a Chip 17, 614–628.
- HE, G.-Y., WANG, Y.-C., TSAO, H.-K. & SHENG, Y.-J. 2024 Wicking dynamics of two-ply channels in porous medium-based microfluidic devices. *Phys. Fluids* **36**, 062115.
- HONG, S. & KIM, W. 2015 Dynamics of water imbibition through paper channels with wax boundaries. *Microfluid. Nanofluid.* 19, 845–853.
- JAFRY, A.T., LIM, H., KANG, S.I., SUK, J.W. & LEE, J. 2016 A comparative study of paper-based microfluidic devices with respect to channel geometry. *Colloids Surf. A: Physicochem. Engng Asp.* 492, 190–198.
- JAHANSHAHI-ANBUHI, S., CHAVAN, P., SICARD, C., LEUNG, V., HOSSAIN, S.M.Z., PELTON, R., BRENNAN, J.D. & FILIPE, C.D.M. 2012 Creating fast flow channels in paper fluidic devices to control timing of sequential reactions. *Lab on a Chip* 12, 5079–5085.
- JANG, I., BERG, K.E. & HENRY, C.S. 2020a Viscosity measurements utilizing a fast-flow microfluidic paperbased device. Sens. Actuators B: Chem. 319, 128240.
- JANG, I., CARRÃO, D.B., MENGER, R.F., MORAES DE OLIVEIRA, A.R. & HENRY, C.S. 2020b Pump-free microfluidic rapid mixer combined with a paper-based channel. ACS Sens. 5, 2230–2238.
- KVICK, M., MARTINEZ, D.M., HEWITT, D.R. & BALMFORTH, N.J. 2017 Imbibition with swelling: capillary rise in thin deformable porous media. *Phys. Rev. Fluids* 2, 074001.
- LEE, M., KIM, S., KIM, H.-Y. & MAHADEVAN, L. 2016 Bending and buckling of wet paper. *Phys. Fluids* 28, 042101.
- LI, L., WESTERBEEK, E.Y., VOLLENBROEK, J.C., DE BEER, S., SHUI, L., ODIJK, M. & EIJKEL, J.C.T. 2021 Autonomous capillary microfluidic devices with constant flow rate and temperature-controlled valving. *Soft Matter* 17, 7781–7791.
- LIU, Z., HE, X., HAN, J., ZHANG, X., LI, F., LI, A., QU, Z. & XU, F. 2018 Liquid wicking behavior in paper-like materials: mathematical models and their emerging biomedical applications. *Microfluid. Nanofluid.* 22, 132
- MARTINEZ, A.W., PHILLIPS, S.T., BUTTE, M.J. & WHITESIDES, G.M. 2007 Patterned paper as a platform for inexpensive, low-volume, portable bioassays. *Angew. Chem.* 119, 1340–1342.
- MARTINEZ, A.W., PHILLIPS, S.T., WHITESIDES, G.M. & CARRILHO, E. 2010 Diagnostics for the developing world: microfluidic paper-based analytical devices. *Anal. Chem.* 82, 3–10.
- OLANREWAJU, A., BEAUGRAND, M., YAFIA, M. & JUNCKER, D. 2018 Capillary microfluidics in microchannels: from microfluidic networks to capillaric circuits. *Lab on a Chip* 18, 2323–2347.
- OZER, T., MCMAHON, C. & HENRY, C.S. 2020 Advances in paper-based analytical devices. *Annu. Rev. Anal. Chem.* 13, 85–109.
- PRADELA-FILHO, L.A., NOVIANA, E., ARAÚJO, D.A.G., TAKEUCHI, R.M., SANTOS, A.L. & HENRY, C.S. 2020 Rapid analysis in continuous-flow electrochemical paper-based analytical devices. ACS Sens. 5, 274–281.
- RENAULT, C., LI, X., FOSDICK, S.E. & CROOKS, R.M. 2013 Hollow-channel paper analytical devices. *Anal. Chem.* 85, 7976–7979.
- SCHAUMBURG, F. & BERLI, C.L.A. 2019 Assessing the rapid flow in multilayer paper-based microfluidic devices. Microfluid. Nanofluid. 23, 98.
- SCHILLING, K.M., LEPORE, A.L., KURIAN, J.A. & MARTINEZ, A.W. 2012 Fully enclosed microfluidic paper-based analytical devices. *Anal. Chem.* 84, 1579–1585.
- SEO, J., JUNG, S., PARK, J., KIM, H.-Y. & KIM, S.J. 2023 Hierarchical capillarity-assisted liquid invasion in multilayered paper channels for nanoelectrokinetic preconcentration. *Nano Lett.* 23, 8065–8072.
- SHANGGUAN, J.-W., LIU, Y., WANG, S., HOU, Y.-X., XU, B.-Y., XU, J.-J. & CHEN, H.-Y. 2018 Paper capillary enables effective sampling for microfluidic paper analytical devices. *ACS Sens.* 3, 1416–1423.
- SONGOK, J. & TOIVAKKA, M. 2016 Enhancing capillary-driven flow for paper-based microfluidic channels. *ACS Appl. Mater. Interfaces* **8**, 30523–30530.
- SOUM, V., PARK, S., BRILIAN, A.I., CHOI, J.-Y., LEE, Y., KIM, W., KWON, O.-S. & SHIN, K. 2020 Quantitatively controllable fluid flows with ballpoint-pen-printed patterns for programmable photo-paper-based microfluidic devices. *Lab on a Chip* **20**, 1601–1611.
- WASHBURN, E.W. 1921 The dynamics of capillary flow. Phys. Rev. 17, 273.
- YETISEN, A.K., AKRAM, M.S. & LOWE, C.R. 2013 Paper-based microfluidic point-of-care diagnostic devices. Lab on a Chip 13, 2210–2251.